axioms

MDPI

Article

Numerical Analysis of Heat Transfer through Hollow Brick Using Finite-Difference Method

Igor V. Miroshnichenko [1,*], Nikita S. Gibanov [2] and Mikhail A. Sheremet [2]

[1] Regional Scientific and Educational Mathematical Centre, Tomsk State University, 634050 Tomsk, Russia
[2] Laboratory on Convective Heat and Mass Transfer, Tomsk State University, 634050 Tomsk, Russia; gibanov@mail.tsu.ru (N.S.G.); sheremet@math.tsu.ru (M.A.S.)
* Correspondence: miroshnichenko@mail.tsu.ru; Tel.: +7-3822-529740

Abstract: The goal of the present work is to develop and test in detail a numerical algorithm for solving the problem of complex heat transfer in hollow bricks. The finite-difference method is used to solve the governing equations. The article also provides a detailed description of the procedure for thickening the computational grid. The flow regime inside the hollow brick is turbulent, which is a distinctive feature of this work. As a rule, if the size of the cavities in the brick is greater than 20 cm and the temperature difference in the considered solution region is significant, then the numerical solution can be obtained in the turbulent approximation. The effect of surface emissivities of internal walls on the thermal transmission and air flow inside hollow brick is investigated. The distributions of isolines of the stream function and temperature are obtained. The results report that the emissivity of interior surfaces significantly affects the heat transfer through hollow bricks.

Keywords: algebraic coordinate transformation; finite-difference method; hollow brick; heat transfer

Citation: Miroshnichenko, I.V.; Gibanov, N.S.; Sheremet, M.A. Numerical Analysis of Heat Transfer through Hollow Brick Using Finite-Difference Method. *Axioms* **2022**, *11*, 37. https://doi.org/10.3390/axioms11020037

Academic Editor: Delfim F. M. Torres

Received: 14 December 2021
Accepted: 14 January 2022
Published: 19 January 2022

1. Introduction

Over the past decades, humanity has been striving to improve the energy efficiency of buildings. This approach will ultimately lead to colossal savings in energy resources. In this regard, it is necessary to use energy-efficient building materials that have proven their effectiveness experimentally and through numerical modeling. Hollow bricks (eco-friendly construction material) are widely utilized in the construction of buildings due to their high thermal resistance. The air inside the brick has a low coefficient of thermal conductivity. Controlling the processes of natural convection inside the brick allows us to control the values of thermal resistance. It is also worth noting that radiative heat transfer also occurs between the walls inside the brick, which also affects the overall heat transfer.

In recent years, many interesting numerical and experimental articles devoted to the investigation of convective-radiative heat transfer have been published [1–6]. The authors used various methods for the numerical solution of problems under consideration: finite-difference method, lattice Boltzmann method, finite-volume method, finite element method, and so on. A detailed review of various methods for solving problems of convective-radiative thermal transmission in enclosures is presented in the work [7]. The authors showed that taking into account radiation as the main mechanism of energy transfer is necessary even for a relatively small temperature difference in the solution region. Singh and Sharif [8] have investigated the mixed convective cooling of a two-dimensional rectangular cavity with differentially heated side walls. Cold liquid is blown into the cavity through an inlet in the side wall of the cavity and exits through an outlet in the opposite side wall. Their findings indicate that maximum cooling effectiveness is achieved if the inlet is kept near the bottom of the cold wall while the outlet is placed near the top of the hot wall.

Numerical analysis of heat transfer processes makes it possible to better understand the mechanisms of energy transfer and estimate the contributions of convection, conduction, and radiation. It is worth noting that if the size of the closed region is large or the temperature difference is significant, then turbulent flows are formed in the closed region. In this case, it is necessary to simulate turbulent flow regimes. To accurately define the velocities and temperature variations inside the boundary layer, the mesh is usually thickened near the walls [9–11]. Such thickening can be performed using the theory of functions of a complex variable.

Over the past decade, several studies have been carried out to investigate heat transfer processes in hollow building materials. Jamal et al. [12] presented a numerical study of the thermal behavior of different types of hollow bricks, which are mainly utilized in the construction of walls in Moroccan buildings. The governing equations in their work are discretized by the finite volume method. Their findings indicated that one of three types of hollow bricks can significantly reduce thermal transmission from the outside to the inside of the building walls and therefore provide adequate thermal comfort. Alhazmy [13] presented the numerical results of a study on the influence of the location and size of two baffles on the free convection inside the hollow bricks. The baffles are attached to the bottom and top sides, dividing the inner area into three parts. It has been shown that long baffles divide the air flow into three various convective cells and the largest magnification of thermal resistance is 53% compared to cavities without baffles.

Two-dimensional thermal transmission by conduction, thermogravitational convection, and infrared radiation inside honeycomb walls separated by air has been studied by Boukendil et al. [14]. Airflow was laminar. The vertical external walls are considered to be isothermal while the top and bottom horizontal surfaces of walls are insulated. Their findings indicated that the overall heat flux through the wall changes almost linearly depending on the difference between the external and internal temperatures. Moreover, heat transfer through the investigated double honeycomb walls is highly dependent on the thermal conductivity of the material from which the hollow bricks are made. Numerical simulation of thermal radiation, thermogravitational convection, and conduction in double hollow brick walls with mortar joints has been carried out by Boukendil et al. [15]. The impact of mortar joint thickness and the emissivity of internal surfaces of bricks on thermal transmission has been predicted for various temperature differences. They have shown that utilizing 1 cm thick mortar is a good compromise for estimating the thickness required to join hollow bricks. Their findings have also indicated that this thickness, together with the low emissivity of the internal walls, can significantly reduce the energy consumption of buildings.

Turbulent regimes of thermogravitational convection and surface radiation in a closed area have been studied numerically by Sharma et al. [16]. The considered solution region is cooled from the top, left and right walls, and heated from below. The standard $k - \varepsilon$ turbulence model has been used. The problem has been solved in dimensionless form. The Rayleigh number is varied from 10^8 to 10^{12}. Correlations are obtained for the Nusselt number which depends on the Rayleigh number and aspect ratio. They have also investigated the impact of external heat transfer coefficient and surface emissivities of internal walls on air flow and thermal transmission. Vivek et al. [17] studied the interaction impacts between radiation and free convection in inclined rectangular cavities. The two opposite walls of the cavity heat up differently, while other walls are considered to be adiabatic. The authors concluded that convection can be suppressed by 50% with a positive slope, while it can be increased by over 100% with a negative slope for an aspect ratio of 5.

From the above literature survey, it can be concluded that numerical studies of thermal transmission processes in hollow building materials are relevant. Most of the calculations have been carried out under laminar conditions, due to the small size of the voids in the bricks. However, in some situations, the characteristic size of hollow structures can reach ten or more centimeters. In this case, it is advisable to consider turbulent models of energy transfer. In this work, all mechanisms of energy transfer will be taken into

account (convection, surface radiation, and conduction). The main aim of this article is to investigate the influence of the surface emissivity of internal walls of the brick and to study the evolution in time of convective structures forming inside the hollow brick.

2. Governing Equations and Numerical Method

The configuration of the hollow brick to be studied is illustrated in Figure 1. Dirichlet boundary conditions are considered on the right and left walls of the brick (the left wall heats up, the right one cools). Horizontal external surfaces are thermally insulated. Inside the brick cavities, there is air, which is considered to be a viscous Newtonian fluid that satisfies the Boussinesq approximation. Thermal transmission and fluid flow are two-dimensional and turbulent. The following assumptions are used for heat transfer by radiation: the medium inside the cavities is diathermic, the internal surfaces of the solid walls radiate diffusely.

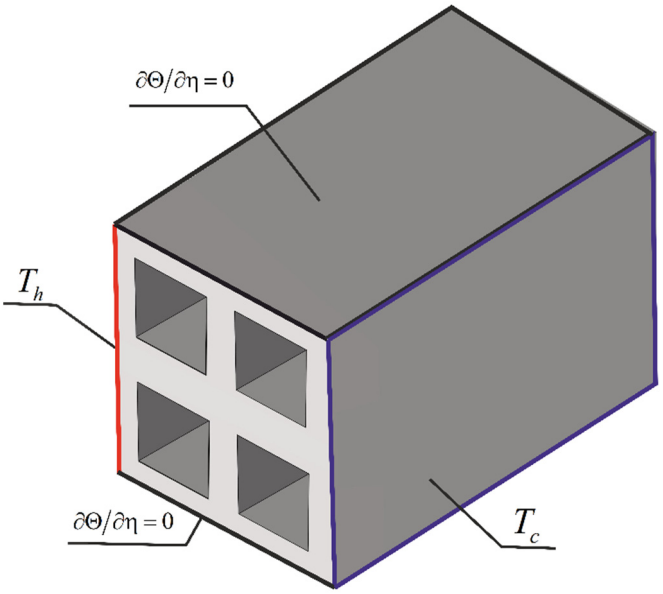

Figure 1. A schematic of the hollow brick.

The governing equations describing the processes of transfer of heat, mass, and momentum inside the voids of a hollow brick, as well as in solid walls, are written as follows:

$$\frac{\partial u}{\partial x} + \frac{\partial v}{\partial y} = 0 \tag{1}$$

$$\frac{\partial u}{\partial t} + u\frac{\partial u}{\partial x} + v\frac{\partial u}{\partial y} = -\frac{1}{\rho}\frac{\partial p}{\partial x} + 2\frac{\partial}{\partial x}\left[(\nu + \nu_t)\frac{\partial u}{\partial x}\right] + \frac{\partial}{\partial y}\left[(\nu + \nu_t)\left(\frac{\partial u}{\partial y} + \frac{\partial v}{\partial x}\right)\right] \tag{2}$$

$$\frac{\partial v}{\partial t} + u\frac{\partial v}{\partial x} + v\frac{\partial v}{\partial y} = -\frac{1}{\rho}\frac{\partial p}{\partial y} + \frac{\partial}{\partial x}\left[(\nu + \nu_t)\left(\frac{\partial u}{\partial y} + \frac{\partial v}{\partial x}\right)\right] + 2\frac{\partial}{\partial y}\left[(\nu + \nu_t)\frac{\partial v}{\partial y}\right] + g\beta(T - T_0) \tag{3}$$

$$\frac{\partial T}{\partial t} + u\frac{\partial T}{\partial x} + v\frac{\partial T}{\partial y} = \frac{\partial}{\partial x}\left[\left(\alpha_{air} + \frac{\nu_t}{\mathrm{Pr}_t}\right)\frac{\partial T}{\partial x}\right] + \frac{\partial}{\partial y}\left[\left(\alpha_{air} + \frac{\nu_t}{\mathrm{Pr}_t}\right)\frac{\partial T}{\partial y}\right] \tag{4}$$

$$\frac{\partial k}{\partial t} + u\frac{\partial k}{\partial x} + v\frac{\partial k}{\partial y} = \frac{\partial}{\partial x}\left[\left(\nu + \frac{\nu_t}{\sigma_k}\right)\frac{\partial k}{\partial x}\right] + \frac{\partial}{\partial y}\left[\left(\nu + \frac{\nu_t}{\sigma_k}\right)\frac{\partial k}{\partial y}\right] + P_k + G_k - \varepsilon \tag{5}$$

$$\frac{\partial \varepsilon}{\partial t} + u\frac{\partial \varepsilon}{\partial x} + v\frac{\partial \varepsilon}{\partial y} = \frac{\partial}{\partial x}\left[\left(\nu + \frac{\nu_t}{\sigma_\varepsilon}\right)\frac{\partial \varepsilon}{\partial x}\right] + \frac{\partial}{\partial y}\left[\left(\nu + \frac{\nu_t}{\sigma_\varepsilon}\right)\frac{\partial \varepsilon}{\partial y}\right] + (c_{1\varepsilon}(P_k + c_{3\varepsilon}G_k) - c_{2\varepsilon}\varepsilon)\frac{\varepsilon}{k} \tag{6}$$

$$\frac{\partial T}{\partial t} = \alpha_w\left(\frac{\partial^2 T}{\partial x^2} + \frac{\partial^2 T}{\partial y^2}\right) \tag{7}$$

The value of the parameters P_k, G_k can be found in [10]. For the $k - \varepsilon$ turbulence model, the values of the constants are presented in Table 1.

Table 1. Parameters of the $k-\varepsilon$ turbulence model.

Parameters	c_{μ}	$c_{1\varepsilon}$	$c_{2\varepsilon}$	$c_{3\varepsilon}$	σ_k	σ_{ε}	$\mathbf{Pr}_t$
Values	0.09	1.44	1.92	0.8	1.0	1.3	1.0

The problem under consideration has been solved in a dimensionless form. The corresponding dimensionless variables have the following form.

$$\begin{gathered} X = x/L, Y = y/L, U = u/\sqrt{g\beta\Delta TL}, \tau = t\sqrt{g\beta\Delta T/L}, \\ \Theta = (T-T_c)/(T_h-T_c), \quad V = v/\sqrt{g\beta\Delta TL}, \Psi = \psi/\sqrt{g\beta\Delta TL^3}, \\ \Omega = \omega\sqrt{L/g\beta\Delta T}, E = \varepsilon/\sqrt{g^3\beta^3(\Delta T)^3L}, \quad K = k/(g\beta\Delta TL). \end{gathered} \tag{8}$$

The problem is solved in terms of the vorticity-stream function due to the fact that the determination of the pressure field is of little interest. Formulas for vorticity as well as stream function are as follows:

$$\frac{\partial V}{\partial X} - \frac{\partial U}{\partial Y} = \Omega, \ \frac{\partial \Psi}{\partial Y} = U, -\frac{\partial \Psi}{\partial X} = V \tag{9}$$

As a result of dimensionlessness, characteristic similarity numbers appear in the governing equations: the Prandtl number and the Rayleigh number. The definition for these dimensionless parameters is as follows:

$$\mathrm{Pr} = \frac{\nu}{\alpha_f}, \ \mathrm{Ra} = \frac{g\beta\Delta TL^3}{\nu\alpha_f}. \tag{10}$$

The Rayleigh number is a dimensionless number that determines the behavior of a fluid under the influence of a temperature gradient. The Prandtl number shows the influence of the thermophysical properties of the coolant on thermal transmission. In this work, the Prandtl number is 0.7.

The investigated 2D configuration, shown in Figure 2, is formed by 4 square enclosures of size L surrounded by solid partitions. The computational grid is refined near the inner surfaces of solid walls. The formula that allows us to thicken the mesh to the walls is given as follows:

$$\begin{gathered} \xi = c + \tfrac{d-c}{2}\left\{1 + \mathrm{tg}\left[\tfrac{\pi\kappa}{d-c}\left(x - \tfrac{c+d}{2}\right)\right]/\mathrm{tg}\left[\tfrac{\pi}{2}\kappa\right]\right\}, \\ \eta = c + \tfrac{d-c}{2}\left\{1 + \mathrm{tg}\left[\tfrac{\pi\kappa}{d-c}\left(y - \tfrac{c+d}{2}\right)\right]/\mathrm{tg}\left[\tfrac{\pi}{2}\kappa\right]\right\}. \end{gathered} \tag{11}$$

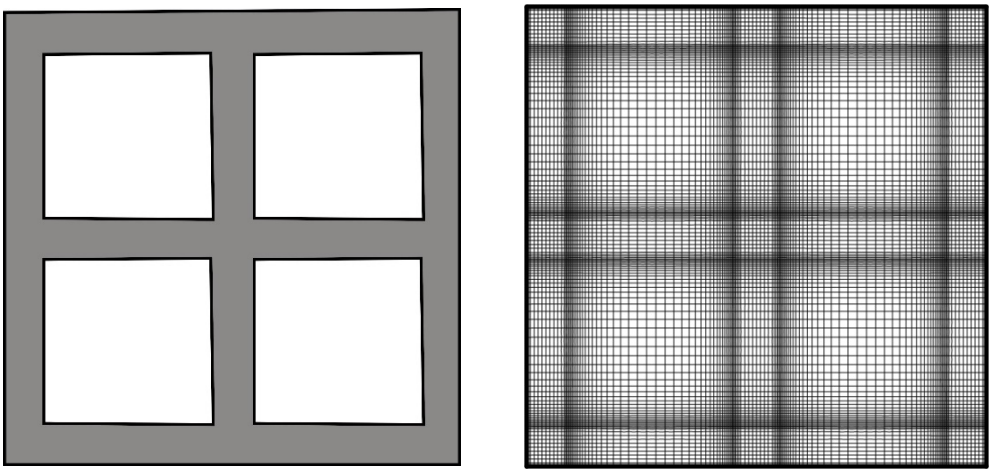

Figure 2. Computational domain and utilized mesh.

Formulas of this type are obtained using the theory of functions of a complex variable. Changing the values of the parameter κ allows us to adjust the level of thickening. The transition from variables

x and y to variables ξ and η allows one to go from a non-uniform grid to a uniform one. The derivatives of the first and second order with respect to coordinates are

$$\begin{array}{ll} \frac{\partial \xi}{\partial x} = \frac{\pi\kappa}{2\mathrm{tg}\left(\frac{\pi\kappa}{2}\right)\cos^2\left(\frac{\pi\kappa}{2}(2x-1)\right)}, & \frac{\partial^2 \xi}{\partial x^2} = \frac{(\pi\kappa)^2}{\mathrm{tg}\left(\frac{\pi\kappa}{2}\right)}\frac{\sin\left(\frac{\pi\kappa}{2}(2x-1)\right)}{\cos^3\left(\frac{\pi\kappa}{2}(2x-1)\right)}, \\ \frac{\partial \eta}{\partial y} = \frac{\pi\kappa}{2\mathrm{tg}\left(\frac{\pi\kappa}{2}\right)\cos^2\left(\frac{\pi\kappa}{2}(2y-1)\right)}, & \frac{\partial^2 \eta}{\partial y^2} = \frac{(\pi\kappa)^2}{\mathrm{tg}\left(\frac{\pi\kappa}{2}\right)}\frac{\sin\left(\frac{\pi\kappa}{2}(2y-1)\right)}{\cos^3\left(\frac{\pi\kappa}{2}(2y-1)\right)}. \end{array} \quad (12)$$

As mentioned earlier in this work, to describe heat transfer due to radiation, the surface radiation model is utilized. To determine the dimensionless radiation flux, it is necessary to solve the equations below by the method of successive over-relaxation.

$$\begin{array}{l} Q_{rad,k} = R_k - \sum\limits_{i=1}^{N} F_{k-i}R_i, \\ R_k = (1-\widetilde{\varepsilon}_k)\sum\limits_{i=1}^{N} F_{k-i}R_i + \widetilde{\varepsilon}_k(1-\zeta)^4\left(\Theta_k + 0.5\frac{1+\zeta}{1-\zeta}\right)^4. \end{array} \quad (13)$$

The boundary conditions for this problem are presented in Table 2.

Table 2. Boundary conditions associated with Equations (1)–(5).

Boundaries	Conditions
Left external wall	$\Theta = 0.5$
Right external wall	$\Theta = -0.5$
Top external wall	$\frac{\partial\Theta}{\partial\eta} = 0$
Bottom external wall	$\frac{\partial\Theta}{\partial\eta} = 0$
Internal surfaces of the solid material and air, parallel to the axis $O\xi$	$\Psi = 0$, $\frac{\partial\Psi}{\partial\eta} = 0$, $\Theta_w = \Theta_{air}$, $\lambda_{w,air}\frac{\partial\eta}{\partial Y}\frac{\partial\Theta_w}{\partial\eta} = \frac{\partial\eta}{\partial Y}\frac{\partial\Theta_{air}}{\partial\eta} - N_{rad}Q_{rad}$;
Internal surfaces of the solid material and air, parallel to the axis $O\eta$	$\Psi = 0$, $\frac{\partial\Psi}{\partial\xi} = 0$, $\Theta_w = \Theta_{air}$, $\lambda_{w,air}\frac{\partial\xi}{\partial X}\frac{\partial\Theta_w}{\partial\xi} = \frac{\partial\xi}{\partial X}\frac{\partial\Theta_{air}}{\partial\xi} - N_{rad}Q_{rad}$.

The governing Equations (1)–(5) with corresponding boundary conditions are solved using the finite-difference method. Different approaches are used to solve parabolic and elliptic equations. For parabolic equations, the scheme is as follows:

(1) Application of the locally one-dimensional scheme of the Samarskii.
(2) Discretization of diffusion and convective terms.
(3) Solving the resulting system of linear algebraic equations using the Thomas algorithm.

When solving elliptic equations, they are discretized before the method of successive over-relaxation is used to solve systems of linear algebraic equations.

Consider the method for solving the Poisson equation for the stream function.

$$\frac{d^2\xi}{dX^2}\frac{\partial\Psi}{\partial\xi} + \left(\frac{d\xi}{dX}\right)^2\frac{\partial^2\Psi}{\partial\xi^2} + \frac{d^2\eta}{dY^2}\frac{\partial\Psi}{\partial\eta} + \left(\frac{d\eta}{dY}\right)^2\frac{\partial^2\Psi}{\partial\eta^2} = -\Omega. \quad (14)$$

To approximate second-order derivatives in elliptic equations, the central differences are used. As a result, we obtain the following discrete equation:

$$\begin{array}{l} \frac{d^2\xi_i}{dX_i^2}\frac{\Psi^k_{i+1,j}-\Psi^{k+1}_{i-1,j}}{2h_\xi} + \left(\frac{d\xi_i}{dX_i}\right)^2\frac{\Psi^k_{i+1,j}-2\Psi^{k+1}_{i,j}+\Psi^{k+1}_{i-1,j}}{h_\xi^2} + \frac{d^2\eta_j}{dY_j^2}\frac{\Psi^k_{i,j+1}-\Psi^{k+1}_{i,j-1}}{2h_\eta} + \\ + \left(\frac{d\eta_j}{dY_j}\right)^2\frac{\Psi^k_{i,j+1}-2\Psi^{k+1}_{i,j}+\Psi^{k+1}_{i,j-1}}{h_\eta^2} = -\Omega_{i,j}, \end{array} \quad (15)$$

where k is the iteration number.

Let's introduce the notation:

$$\frac{d\xi_i}{dX_i} = a, \quad \frac{d^2\xi_i}{dX_i{}^2} = b, \quad \frac{d\eta_j}{dY_j} = c, \quad \frac{d^2\eta_j}{dY_j{}^2} = d. \quad (16)$$

Next, the system of algebraic linear equations is solved by the method of successive over-relaxation:

$$\begin{cases} \overset{\frown}{\Psi}{}^{k+1}_{i,j} = \frac{h_\eta^2 h_\xi b\left(\Psi^k_{i+1,j}-\Psi^{k+1}_{i-1,j}\right)}{4\left(c^2h_\xi^2+a^2h_\eta^2\right)} + \frac{h_\eta^2\left(\Psi^k_{i+1,j}+\Psi^{k+1}_{i-1,j}\right)}{2\left(c^2h_\xi^2+a^2h_\eta^2\right)} + \frac{h_\xi^2 h_\eta d\left(\Psi^k_{i,j+1}-\Psi^{k+1}_{i,j-1}\right)}{4\left(c^2h_\xi^2+a^2h_\eta^2\right)} + \\ + \frac{h_\xi^2\left(\Psi^k_{i,j+1}+\Psi^{k+1}_{i,j-1}\right)}{2\left(c^2h_\xi^2+a^2h_\eta^2\right)} + \frac{h_\xi^2 h_\eta^2\Omega_{i,j}}{2\left(c^2h_\xi^2+a^2h_\eta^2\right)}, \\ \Psi^{k+1}_{i,j} = \Psi^k_{i,j} + \varpi\left(\overset{\frown}{\Psi}{}^{k+1}_{i,j} - \Psi^k_{i,j}\right), \end{cases} \tag{17}$$

where h_ξ, h_η are grid steps by coordinates ξ and η, respectively.

The relaxation parameter ϖ has been chosen empirically from the results of many numerical calculations. It should be noted that at each time step, it is required to carry out calculations for Ψ to complete the convergence of the iterative process. The convergence condition is given as follows:

$$\max_{i,j}\left|\Psi^{k+1}_{i,j} - \Psi^k_{i,j}\right| < \hat{\varepsilon}. \tag{18}$$

where $\hat{\varepsilon}$ determines the required accuracy of calculations. Detailed analysis of the effect of mesh size was also carried out. Three different meshes of 60 × 60, 120 × 120, and 180 × 180 are used to validate the mesh independence. The average convective and radiative Nusselt numbers at the right bottom vertical wall and fluid flow rate at Ra = 0.5×10^8, $\widetilde{\varepsilon} = 0.8$ are presented in Table 3. As a result of the analysis, a non-uniform 120 × 120 mesh was chosen for the solution.

Table 3. Mesh independence analysis.

Grid Size	$\mathbf{Nu_{conv}}$	$\mathbf{Nu_{rad}}$
60 × 60	6.54	6.46
120 × 120	8.63	6.61
180 × 180	8.71	6.67

The developed solution method has been tested in detail on a variety of heat transfer problems in closed areas. Figure 3 show the temperature fields and isolines of stream functions for the case of convective-radiative thermal transmission in a closed, differentially heated region. The results obtained are in good agreement with the results from the work of Wang et al. [18]. Figure 4 show a comparison of the profiles temperature and horizontal velocity from the work of Wang et al. [18].

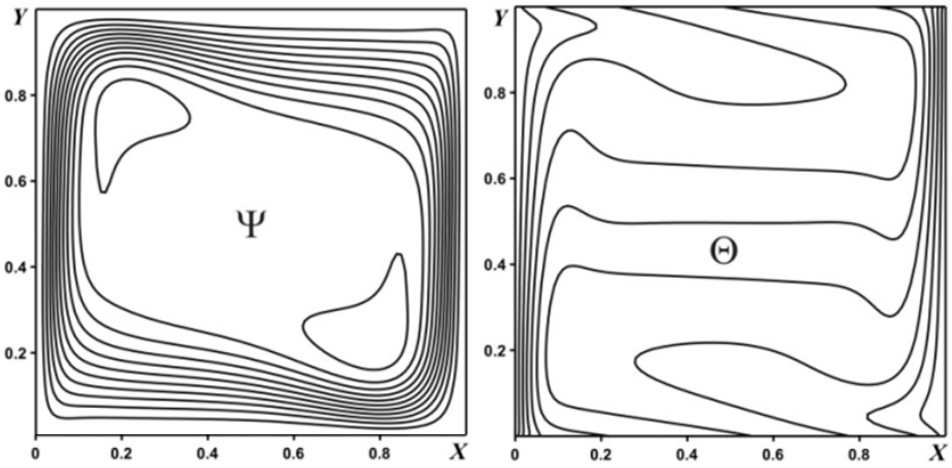

Figure 3. Streamlines Ψ and isotherms Θ.

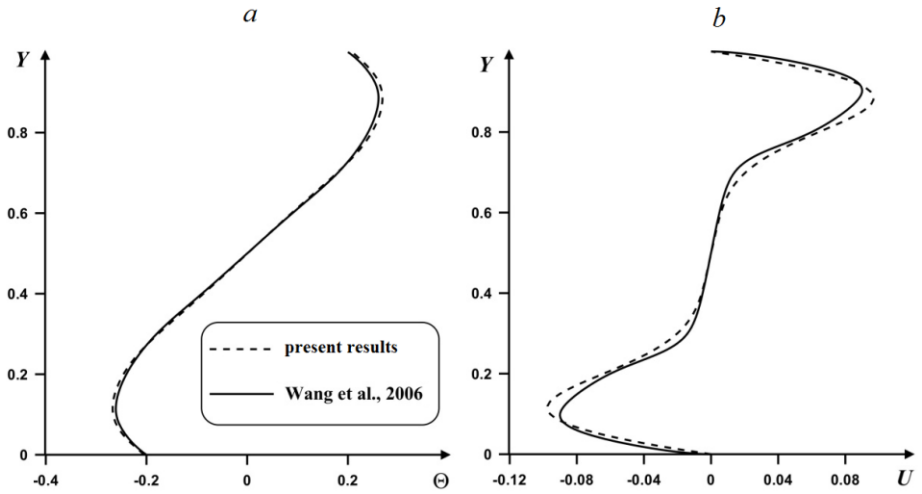

Figure 4. Profiles of temperature (**a**) and horizontal velocity (**b**) at $X = 0.5$, in comparison with data of Wang et al. [18].

To verify the developed program code, a comparison with the experimental work of Ampofo and Karayiannis [19] has also been carried out. Figure 5 shows the temperature and vertical velocity profiles at Rayleigh number Ra = 1.58×10^9. It should be noted that the agreement is very good.

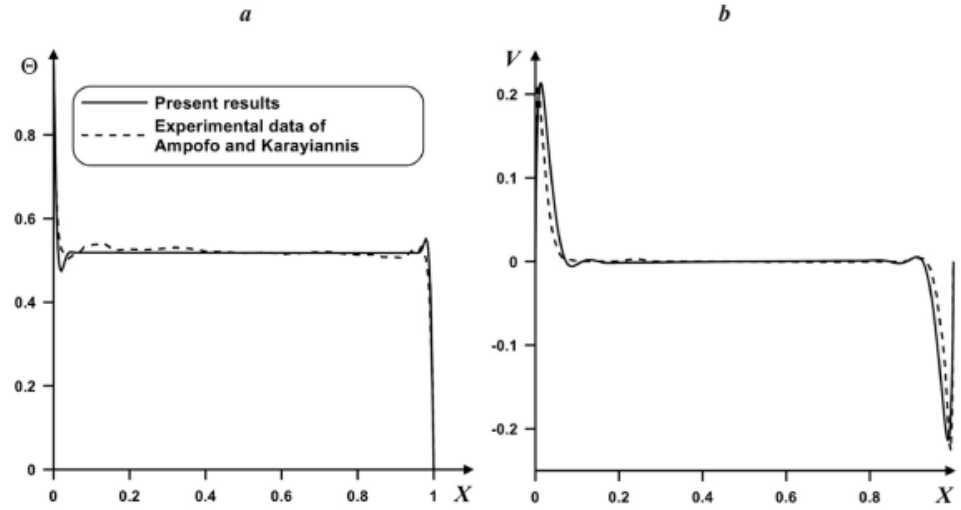

Figure 5. The temperature profiles (**a**) and vertical velocity profiles (**b**).

3. Results

In real practical situations, the dimensions of voids and wall thicknesses in the hollow brick are constant. Therefore, the real thermal state of the investigated object is determined by the temperature difference, the thermal conductivity coefficients of the medium and walls, as well as the surface emissivities of the inner surfaces of the solid walls. The influence of the latter parameter on thermal transmission and air flow, according to the author of the work, has not been sufficiently studied. In this connection, the main aim of this work is to study the effect of the surface emissivity of internal walls of the brick on the distribution of integral and local parameters. In the present section, the numerical results have been reported for Ra = 0.5×10^8, $\zeta = 0.92$, Pr = 0.7, $N_{rad} = 112.2$, $\tau = 10{,}000$, and $\widetilde{\varepsilon} = 0 - 0.8$.

The study of the evolution in time of thermal and hydrodynamic structures is extremely important. The development in time of the temperature fields and isolines of the stream function helps to better understand the processes of convective vortices formation in voids and to trace the time of penetration of the temperature wave from the outside. Figure 6 shows two-dimensional temperature fields at $\widetilde{\varepsilon} = 0$ for different values of the dimensionless time τ. At the initial time, conduction is the governing mechanism of heat transfer. Heat penetrates the hollow brick through the side walls. Further, convective flows arise in voids due to the temperature difference.

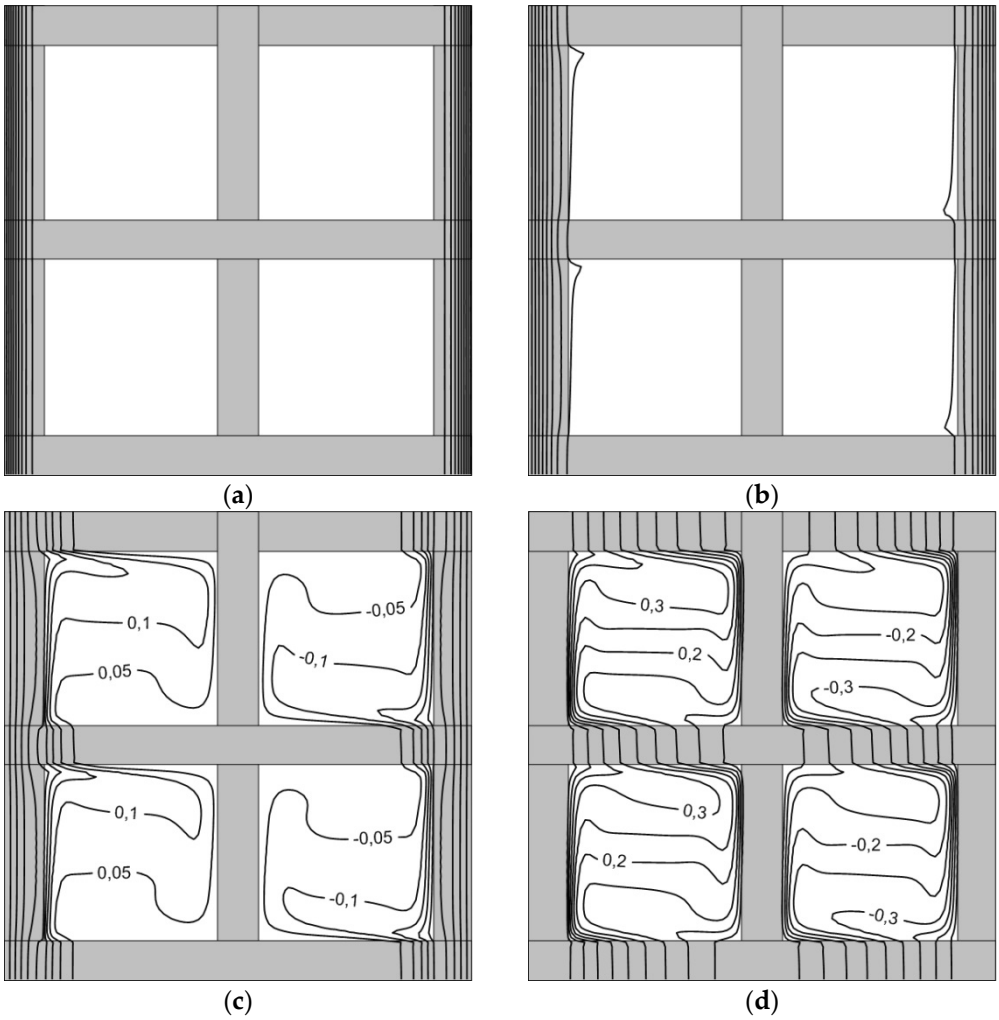

Figure 6. Isotherms Θ at for ζ = 0.92, Ra = 0.5 $\times$ 10^8, Pr = 0.7, $\widetilde{\varepsilon} = 0$: τ = 200 (**a**), τ = 500 (**b**), τ = 1000 (**c**), τ = 10,000 (**d**).

The velocity and temperature fields at τ = 10,000, $\widetilde{\varepsilon} = 0$ are shown in Figure 7. Isotherm stratification is observed in the central part of each void due to differential heating (cooling) of the solution region. A thermal boundary layer forms along the internal vertical walls. It should be noted that the average temperature in the upper left void is higher than in the lower left. This is primarily due to the mechanisms of natural convection and heat conduction due to the transfer of energy from the lower void to the upper one. This can be seen if you look at the position of the isotherm $\Theta = 0.3$ in Figure 7a. The movement of air masses occurs in the same directions for each space in a hollow brick, i.e., the clockwise motion can be found. This is due to the geometry of the solution region, as well as heating and cooling of the external left and right walls.

The total thermal transmission across the internal vertical walls is characterized by Nusselt number. The average convective and radiative Nusselt numbers show a contribution of free convection and radiation in total thermal transmission. For example, the convective and radiative Nusselt numbers on the lower left vertical wall are calculated as:

$$\mathrm{Nu}_{\mathrm{conv}} = \frac{1}{0.45}\int_{0.1}^{0.55}\left|\frac{\partial\xi}{\partial X}\frac{\partial\Theta}{\partial\xi}\right|_{X=0.1} d\eta, \quad \mathrm{Nu}_{\mathrm{rad}} = \frac{\mathrm{N}_{\mathrm{rad}}}{0.45}\int_{0.1}^{0.55}|Q_{rad}|_{X=0.1} d\eta. \tag{19}$$

Average Nusselt numbers have been defined at four boundaries (see Figure 8).

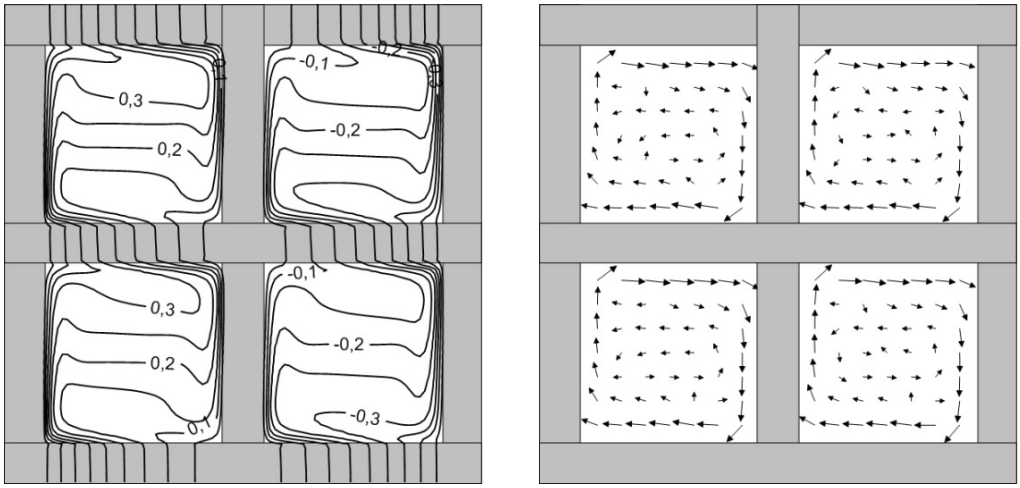

Figure 7. Isotherms Θ (**a**) and velocity field (**b**) for τ = 10,000, $\widetilde{\varepsilon} = 0$.

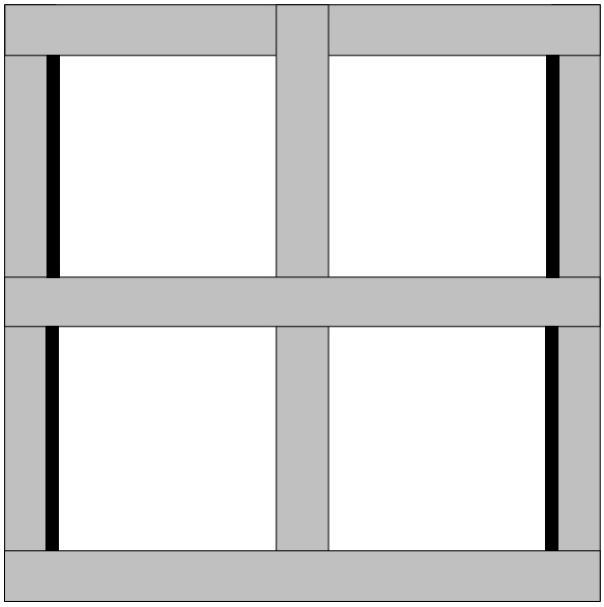

Figure 8. The four boundaries at which the Nusselt number is defined.

In Figure 9, variations of average radiative Nusselt number at the lower left vertical wall are shown. It can be seen that with an increase in the emissivity of surfaces, the average radiative Nusselt number increases significantly. At τ = 10,000, Nu_{rad} is increased to 37% with the changing of surface emissivity from 0.6 to 0.8.

Table 4 presents variations of average convective Nusselt number Nu_{conv}, maximum absolute magnitude of the stream function $|\Psi|_{max}$, and average radiative Nusselt number Nu_{rad}. It can be seen that with an increase in the values of the emissivity of surfaces, a characteristic decrease in the intensity of convective thermal transmission is observed. This also leads to a decrease in the maximum values of the stream function. It should be noted that at high values of $\widetilde{\varepsilon}$, the contribution of radiative heat transfer to the total heat transfer is significant. Therefore, when simulating the processes of heat and mass transfer in hollow building elements, it is necessary to take into account the radiation between the inner surfaces.

Figure 10 shows a comparison of local parameters (isolines of stream function and isotherms) depending on the emissivity of internal surfaces $\widetilde{\varepsilon}$. It can be seen that the hydrodynamic structure of the flow has changed insignificantly. The change in isotherms near solid inner walls is difficult to assess visually. However, detailed calculations show that the temperature field changes with increasing emissivity of the surfaces. This is due to the fact that thermal radiation is perceived by

the internal walls, the temperature of which increases due to such contact, which, as a result, is reflected in the intensity of movement of the medium near these walls. This fact leads to a change in hydrodynamic and thermal parameters of the entire brick (due to the mechanism of convective heat transfer).

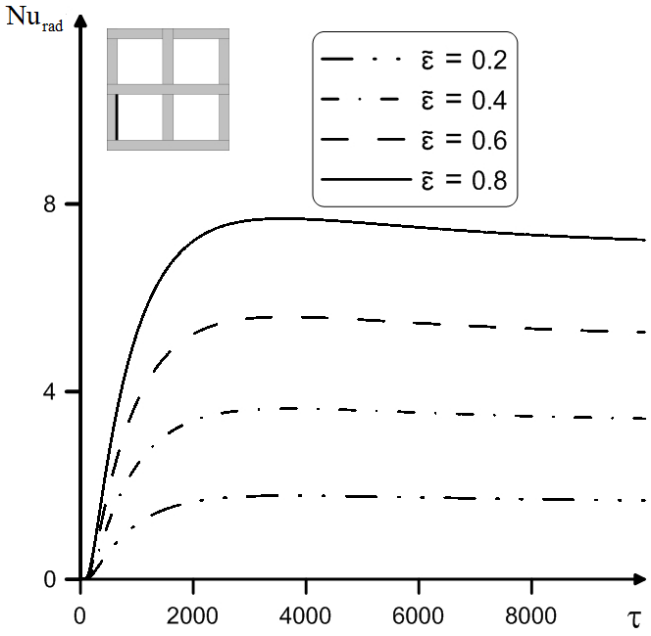

Figure 9. Variations of average radiative Nusselt number with time for different surface emissivities of the lower left vertical wall.

Table 4. Changes of characteristics with $\widetilde{\varepsilon}$ at the right bottom vertical wall for τ = 10,000.

Emissivity of Surfaces	Nu_{conv}	$\lvert \Psi \rvert_{max}$	Nu_{rad}
0.2	9.95	0.00675	1.47
0.4	8.88	0.00670	3.04
0.6	8.77	0.00663	4.73
0.8	8.63	0.00656	6.61

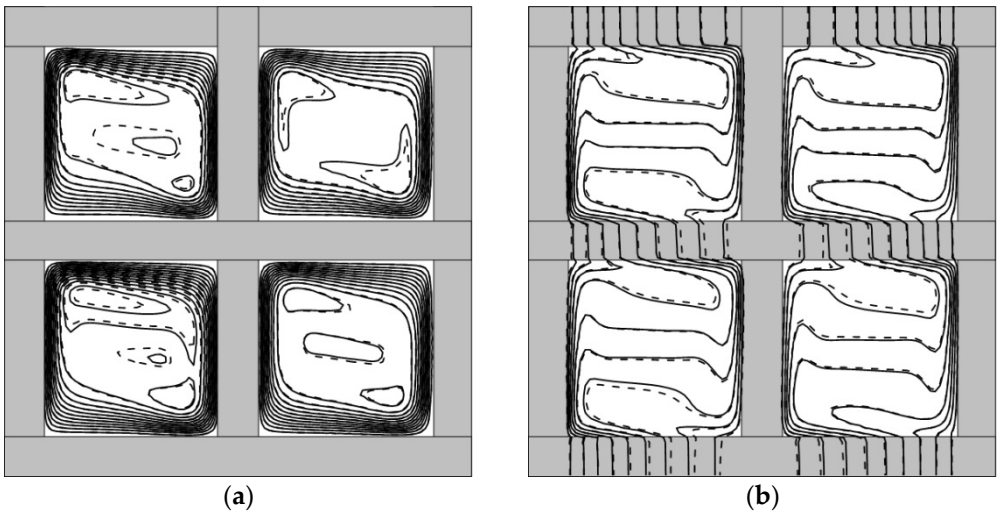

(**a**) (**b**)

Figure 10. Streamlines Ψ (**a**) and Isotherms Θ (**b**) for τ = 10,000: $\widetilde{\varepsilon} = 0.8$-dashed line, $\widetilde{\varepsilon} = 0$ -solid line.

4. Conclusions

The numerical analysis of heat transfer by conduction, free convection, and surface radiation through the hollow brick has been conducted. A mathematical model based on the finite-difference approach was developed to investigate the impact of radiation on the total heat transfer. The system of dimensionless governing equations has been solved in "vorticity-stream function" formulation. To thicken the computational grid to the walls, a special algebraic transformation of coordinates was used. As a result of numerical calculations, the distribution of integral (Nusselt numbers) and local (isotherms and streamlines) parameters has been obtained. A characteristic decrease in the intensity of convective heat transfer with an increase in the emissivity of the inner surfaces of solid walls was shown. Average radiative Nusselt number increased up to 37% with the changing of surface emissivity from 0.6 to 0.8. The use of hollow bricks with a low emissivity of internal surfaces will significantly reduce the energy consumption of buildings.

Author Contributions: I.V.M. and M.A.S. conceived the main concept. I.V.M., M.A.S. and N.S.G. contributed to the investigation and data analysis. I.V.M. wrote the manuscript. All authors contributed to the writing of the final manuscript. All authors have read and agreed to the published version of the manuscript.

Funding: This work was supported by the Ministry of Science and Higher Education of Russia (agreement No. 075-02-2021-1392).

Conflicts of Interest: The authors declare no conflict of interest.

Nomenclature

F_{k-i}	view factor from *k*-th element to the *i*-th element of an enclosure
L	void size (m)
g	acceleration of gravity (m/s^2)
$\widetilde{h}$	heat-transfer coefficient (W/m^2 K)
k	dimensional turbulence kinetic energy (m^2/s^2)
h	thickness of walls (m)
K	dimensionless turbulent kinetic energy
G_k	dimensionless generation/destruction of buoyancy turbulent kinetic energy
E	dimensionless dissipation rate of turbulent kinetic energy
l	height of the heater (m)
$\mathrm{Ra} = g\beta(T_h - T_c)L^3/\nu\alpha_{air}$	Rayleigh number
$\mathrm{Nu_{con}}$	average convective Nusselt number
$\mathrm{N_{rad}} = \sigma T_h^4 L/[\lambda_{air}(T_h - T_c)]$	radiation number
$\mathrm{Pr} = \nu/\alpha_{air}$	Prandtl number
$\mathrm{Nu_{rad}}$	average radiative Nusselt number
P_k	dimensionless shearing production
$\mathrm{Pr}_t = \nu_t/\alpha_t$	turbulent Prandtl number
R_k	dimensionless radiosity of the *k*-th element of an enclosure
Q_{rad}	dimensionless net radiative heat flux
T_h	temperature on the left wall (K)
t	dimensional time (s)
T_c	temperature on the right wall (K)
T	dimensional temperature (K)
Θ_f	dimensionless temperature of fluid
Θ	dimensionless temperature
u,v	dimensional velocity components along X and Y axis (m/s)
Θ_w	dimensionless temperature of wall
X, Y	dimensionless Cartesian coordinates
U, V	dimensionless velocity components along X and Y axis

Greek symbols	
ε	dimensional dissipation rate of turbulent kinetic energy (m^2/s^3)
$\zeta = T_c/T_h$	temperature parameter
β	coefficient of volumetric thermal expansion (1/K)
α_{air}	air thermal diffusivity (m^2/s)
α_w	thermal diffusivity of the wall material (m^2/s)
$\alpha_{i,j} = \alpha_i/\alpha_j$	the thermal diffusivity ratio
$\widetilde{\varepsilon}$	surface emissivity of wall surfaces
λ_{air}	air thermal conductivity (W/m K)
λ_w	thermal conductivity of the wall material (W/m K)
$\lambda_{i,j} = \lambda_i/\lambda_j$	the thermal conductivity ratio
ν	kinematic viscosity (m^2/s)
ψ	dimensional stream function (m^2/s)
ω	dimensional vorticity (s^{-1})
ν_t	turbulent viscosity (m^2/s)
Ψ	dimensionless stream function
ξ, η	new dimensionless independent variables
Ω	dimensionless vorticity
τ	dimensionless time
σ	Stefan–Boltzmann constant ($W/m^2\ K^4$)

References

1. Kogawa, T.; Okajima, J.; Sakurai, A.; Komiya, A.; Maruyama, S. Influence of radiation effect on turbulent natural convection in cubic cavity at normal temperature atmospheric gas. *Int. J. Heat Mass Transfer.* **2017**, *104*, 456–466. [CrossRef]
2. Wang, Y.; Menga, X.; Yangc, X.; Liu, J. Influence of convection and radiation on the thermal environment in an industrial building with buoyancy-driven natural ventilation. *Energy Build.* **2014**, *75*, 394–401. [CrossRef]
3. Shati, A.K.A.; Blakey, S.G.; Beck, S.B.M. A dimensionless solution to radiation and turbulent natural convection in square and rectangular enclosures. *J. Eng. Sci. Technol.* **2012**, *7*, 257–279.
4. Rahimi, M.; Sabernaeemi, A. Experimental study of radiation and free convection in an enclosure with a radiant ceiling heating system. *Energy Build.* **2010**, *42*, 2077–2082. [CrossRef]
5. Ibrahim, A.; Saury, D.; Lemonnier, D. Coupling of Turbulent Natural Convection with Radiation in an Air-Filled Differentially-Heated Cavity at Ra = 1.5×10^9. *Comput. Fluids* **2013**, *88*, 115–125. [CrossRef]
6. Rodriguez Muñoz, N.A.; Briceño Ahumada, Z.C.; Hinojosa Palafox, J.F. Numerical study of heat transfer by convection and thermal radiation in a ventilated room with human heat generation and CO_2 production. *Lat. Am. Appl. Res.* **2013**, *43*, 353–361.
7. Miroshnichenko, I.V.; Sheremet, M.A. Turbulent Natural Convection Heat Transfer in Rectangular Enclosures Using Experimental and Numerical Approaches: A Review. *Renew. Sustain. Energy Rev.* **2018**, *82*, 40–59. [CrossRef]
8. Singh, S.; Sharif, M.A.R. Mixed convective cooling of a rectangular cavity with inlet and exit openings on differentially heated side walls. *Numer. Heat Transfer Part A Appl.* **2003**, *44*, 233–253. [CrossRef]
9. Lari, K.; Baneshi, M.; Gandjalikhan Nassab, S.A.; Komiya, A.; Maruyama, S. Combined heat transfer of radiation and natural convection in a square cavity containing participating gases. *Int. J. Heat Mass Transfer.* **2011**, *54*, 5087–5099. [CrossRef]
10. Miroshnichenko, I.V.; Sheremet, M.A. Turbulent Natural Convection and Surface Radiation in a Closed Air Cavity with a Local Energy Source. *J. Eng. Phys. Thermophys.* **2017**, *90*, 557–563. [CrossRef]
11. Miroshnichenko, I.V.; Toilibayev, A.A.; Sheremet, M.A. Simulation of Thermal Radiation and Turbulent Free Convection in an Enclosure with a GlassWall and a Local Heater. *Fluids* **2021**, *6*, 91. [CrossRef]
12. Jamal, B.; Boukendil, M.; El Moutaouakil, L.; Abdelbaki, A.; Zrikem, Z. Thermal analysis of hollow clay bricks submitted to a sinusoidal heating. *Mater. Today Proc.* **2021**, *45*, 7399–7403. [CrossRef]
13. Alhazmy, M.M. Internal baffles to reduce the natural convection in the voids of hollow blocks. *Build. Simul.* **2010**, *3*, 125–137. [CrossRef]
14. Boukendil, M.; Abdelbaki, A.; Zrikem, Z. Detailed numerical simulation of coupled heat transfer by conduction, natural convection and radiation through double honeycomb walls. *Build. Simul.* **2012**, *5*, 337–344. [CrossRef]
15. Boukendil, M.; Abdelbaki, A.; Zrikem, Z. Numerical simulation of coupled heat transfer through double hollow brick walls: Effects of mortar joint thickness and emissivity. *Appl. Therm. Eng.* **2017**, *125*, 1228–1238. [CrossRef]
16. Sharma, A.K.; Velusamy, K.; Balaji, C. Turbulent Natural Convection in an Enclosure with Localized Heating from Below. *Int. J. Therm. Sci.* **2007**, *46*, 1232–1241. [CrossRef]
17. Vivek, V.; Sharma, A.K.; Balaji, C. Interaction effects between laminar natural convection and surface radiation in tilted square and shallow enclosures. *Int. J. Therm. Sci.* **2012**, *60*, 70–84. [CrossRef]

18. Wang, H.; Xin, S.; Le Quere, P. Numerical study of natural convection-surface radiation coupling in air-filled square cavities. *Comptes Rendus Mec.* **2006**, *334*, 48–57. [CrossRef]
19. Ampofo, F.; Karayiannis, T.G. Experimental benchmark data for turbulent natural convection in an air filled square cavity. *Int. J. Heat Mass Transf.* **2003**, *46*, 3551–3572. [CrossRef]